Model-Based Reconstruction Integrated With Fluence Compensation for Photoacoustic Tomography

Shuhui Bu, *Member, IEEE*, Zhenbao Liu*, *Member, IEEE*, Tsuyoshi Shiina, *Member, IEEE*, Kengo Kondo, Makoto Yamakawa, *Member, IEEE*, Kazuhiko Fukutani, Yasuhiro Someda, and Yasufumi Asao

***Abstract*—Photoacoustic (PA) tomography (PAT) is a rapidly developing imaging modality that can provide high contrast and spatial-resolution images of light-absorption distribution in tissue. However, reconstruction of the absorption distribution is affected by nonuniform light fluence. This paper introduces a reconstruction method for reducing amplification of noise and artifacts in low-fluence regions. In this method, fluence compensation is integrated into model-based reconstruction, and the absorption distribution is iteratively updated. At each iteration, we calculate the residual between detected PA signals and the signals computed by a forward model using the initial pressure, which is the product of estimated voxel value and light fluence. By minimizing the residual, the reconstructed values converge to the true absorption distribution. In addition, we developed a matrix compression method for reducing memory requirements and accelerating reconstruction speed. The results of simulation and phantom experiments indicate that the proposed method provides a better contrast-to-noise ratio (CNR) in low-fluence regions. We expect that the capability of increasing imaging depth will broaden the clinical applications of PAT.**

***Index Terms*—Fluence compensation, model-based reconstruction, photoacoustic (PA).**

I. Introduction

THE photoacoustic (PA) effect [1]–[3] means the generation of acoustic waves by the absorption of electromagnetic (EM) energy. In photoacoustic tomography (PAT), by illuminating a target with a short pulse laser, stress waves are produced due to the thermoelastic expansion. Acoustic sensors are placed at surrounding positions to detect PA signals, and then the absorption source is recovered from the detected PA signals through a reconstruction algorithm. PAT combines the advantages of optical and acoustical methods: sensitive optical absorption contrast and low acoustic scattering in soft tissue. Because light energy is converted to ultrasound that has much less absorption and scattering than light, PAT has much better spatial resolution than traditional optical modalities at depths exceeding the optical ballistic regime. The hemoglobin molecule in blood is a primary absorber in tissue; hence, the absorbed optical-energy distribution reconstructed by PAT can provide the local structure of blood circulation. In the early stage of cancer, capillary vessel density increases. Thus, PAT could detect cancer, especially the breast cancer.

Reconstruction algorithms for PAT have been extensively studied in recent decades [1], [2]. The simplest reconstruction method is delay and sum [4], which is a basic beam-forming technique used in ultrasound imaging. Further improvement can be achieved by utilizing the coherence factor [5] and the minimum variance method [6]. A filtered back-projection (FBP) method [7], [8] is based on inverse Radon transformation [9] and assumes that an object is located near the center of scanning area and far away from detectors. These methods have the advantage of convenient and fast calculation. When the projection data are collected in full view, the FBP algorithm can reconstruct good-quality images with a high signal-to-noise ratio (SNR). However, if the collected data are not in full view, artifacts appear in the reconstructed images. Besides the approximation methods, analytic reconstruction methods with fewer assumptions are proposed to obtain exact reconstruction, for example, universal back-projection (UBP) methods [10], [11] and Fourier domain reconstruction methods [12]–[14]. These analytic reconstruction methods also require enclosed detection for circular scanning or an unbounded open surface for planar scanning, which are generally difficult to implement in a clinical situation. To overcome the limited-view problem, model-based reconstruction methods [15]–[23] (also called iterative reconstruction methods) have been investigated. In these methods, the inverse problem is converted into solving an optimization problem by minimizing the error between detected PA signals and calculated signals from a forward model. In general, although this type of methods needs more computation, it needs fewer detecting sensors and, thus, less acquisition time. It is also able to model nonideal physical conditions and measurement environments. Therefore, the degradation of reconstructed images caused by acoustic inhomogeneity and attenuation can be resolved.

One major problem with PAT reconstruction is that the reconstructed information is affected by nonuniform light fluence,

Manuscript received May 18, 2011; revised September 7, 2011 and December 26, 2011; accepted February 4, 2012. Date of publication February 13, 2012; date of current version April 20, 2012. This work was supported in part by the Innovative Techno-Hub for Integrated Medical Bio-Imaging Project of the Special Coordination Funds, from the Ministry of Education, Culture, Sports, Science, and Technology (MEXT), Japan, and in part by the Natural Science Foundation of China (NSFC) (61003137) and the Scientific Research Foundation (SRF) for Returned Overseas Chinese Scholars (ROCS) and Northwestern Polytechnical University (NWPU) fundamental fund. *Asterisk indicates corresponding author.*

S. Bu is with the Northwestern Polytechnical University, Xian 710072, China, and also with the Kyoto University, Kyoto 606-8501, Japan (e-mail: bushuhui@nwpu.edu.cn).

*Z. Liu is with the Northwestern Polytechnical University, Xian 710072, China (e-mail: liuzhenbao@nwpu.edu.cn).

T. Shiina, K. Kondo, and M. Yamakawa are with Kyoto University, Kyoto 606-8501, Japan (e-mail: shiina@hs.med.kyoto-u.ac.jp; k-kondo@hs.med.kyoto-u.ac.jp; m.yamakawa@kt8.ecs.kyoto-u.ac.jp).

K. Fukutani, Y. Someda, and Y. Asao are with the Medical Imaging Project, Canon Inc., Tokyo 146-8501, Japan (e-mail: fukutani.kazuhiko@canon.co.jp; someda.yasuhiro@canon.co.jp; asao.yasufumi@canon.co.jp).

Color versions of one or more of the figures in this paper are available online at http://ieeexplore.ieee.org.

Digital Object Identifier 10.1109/TBME.2012.2187649

because tissue absorbs and scatters light so that light fluence decreases along the direction of light penetration. The pixels or voxels in reconstructed PAT images are used to represent the level of absorbed optical energy, which is the product of absorption coefficient and light fluence. Therefore, the contrast-to-noise ratio (CNR) in a low-fluence region of a reconstructed image is low. Cox *et al*. [24] proposed a simple iterative method for quantitative reconstruction, where the fluence compensation is performed after image reconstruction. Since the CNR in low-fluence regions in the reconstructed images is low, amplification of the image pixels also amplifies noise and artifacts, which leads to decrease in the image quality. Yuan *et al*. [25] proposed a quantitative reconstruction method using a diffusion equation based on the regularized Newton method. However, the PAT images need segmenting in order to obtain prior structural information. Cox *et al*. [26] extended their work [24] so that chromophore distributions can be estimated by using multiwavelength excitation and gradient-based optimization. Rosenthal *et al*. [27], [28] proposed a sparse representation method for quantitative reconstruction based on the different spatial distribution properties of light fluence and absorption. Although this method does not require the parameter-based fluence distribution, errors occur under nonuniform boundary illumination. Zemp [29] proposed a method for quantitative reconstruction using multiple optical sources even when the Grüneisen coefficient varies spatially, while the reconstruction and transducer bandwidth in this method must be ideal. Their recent research [30] relaxed the limitation of an ideal transducer bandwidth to a more general case.

Because the light fluence, absorption, and scattering coefficient distribution, and even the Grüneisen coefficient are unknown, quantitative reconstruction is highly underdetermined. Therefore, it is very difficult to reconstruct an accurate absorption distribution. In this study, we focus on fluence compensation in order to achieve much clearer reconstruction in low-fluence regions by assuming that the Grüneisen coefficient is constant in the region of interest (ROI) and that the background absorption and scattering distribution are approximately known. Although the reconstructed absorption value is not accurate, the improved imaging depth will greatly facilitate clinical diagnosis. Our proposed method integrates fluence compensation into model-based reconstruction in order to avoid degrading image quality in low-fluence regions due to amplification of noise and artifacts. In contrast with conventional model-based reconstruction methods [15]–[17], the image reconstructed by this method is the absorption distribution. Because feedback is performed at each iteration, the amplification of noise and artifacts can be minimized. The advantages of the proposed method are that reconstruction can be performed under arbitrary illumination conditions, fewer assumptions are required, and noise and artifacts in low-fluence regions of the reconstructed images are reduced. In addition, this method can inherit the merits of the model-based reconstruction method, such as fewer limited-view artifacts [15], fewer artifacts due to nonuniform sound speed [18], and less degradation in lateral resolution [22], [23]. The results of simulation and phantom experiments indicate that the proposed method performs better than conventional methods.

Our proposed method belongs to model-based reconstruction, and such reconstruction requires a large amount of memory and a long calculation time. In order to overcome these limitations, we developed matrix compression methods. By utilizing these methods, the matrix can be compressed to 1/250 its size; hence, our proposed reconstruction method can be implemented with a conventional computer at a high speed.

The rest of this paper is organized as follows. Section II presents the principle of the proposed method. The numerical simulation and phantom experiments are described in Section III. We discuss our overall findings in Section IV. Finally, we conclude our study in Section V.

II. Method

A. Theory of Fluence Compensation and Reconstruction

A PA wave generated in an acoustically homogenous and nonviscous medium can be described as [31], [32]

$$\nabla^2 p(\mathbf{r},t) - \frac{1}{v_s^2}\frac{\partial^2}{\partial t^2}p(\mathbf{r},t) = -\frac{\beta}{C_p}\frac{\partial}{\partial t}H(\mathbf{r},t) \tag{1}$$

where $H(\mathbf{r},t)$ is a heating function defined as the thermal energy converted at position $\mathbf{r}$ and time t by EM radiation per unit volume per unit time, C_p is the isobaric specific heat, β is the coefficient of isobaric volume expansion, and v_s is acoustic speed.

The amount of heat generated in tissue is generally proportional to the input light intensity and the absorption coefficient

$$H(\mathbf{r},t) = \mu_a(\mathbf{r})\Phi(\mathbf{r},t). \tag{2}$$

Here, μ_a is the absorption coefficient, and Φ is the optical fluence. Under the conditions of both thermal and stress confinement, the heating time can be treated as a delta function, such as $H(\mathbf{r},t) \approx \mu_a(\mathbf{r})\Phi(\mathbf{r})\delta(t)$. The initial pressure p_0 of the absorber at position $\mathbf{r}$ can be calculated by

$$\begin{aligned} p_0(\mathbf{r}) &= \frac{v_s^2\beta}{C_p}\mu_a(\mathbf{r})\Phi(\mathbf{r}) \\ &= \Gamma\mu_a(\mathbf{r})\Phi(\mathbf{r}) \end{aligned} \tag{3}$$

where Γ is the Grüneisen coefficient expressed as $\Gamma = \beta v_s^2/C_p$. Here, we assume that the Grüneisen coefficient is constant in the imaging ROI.

Wave equation (1) can be solved by using a Green function approach [1]. Under acoustic stress confinement, the heating process is treated approximately as a Dirac delta function, and the solution is

$$p(\mathbf{r},t) = \frac{\beta}{4\pi C_p}\frac{\partial}{\partial t}\int_V d\mathbf{r}'\frac{\mu_a(\mathbf{r}')\Phi(\mathbf{r}')}{|\mathbf{r}-\mathbf{r}'|}\delta\left(t - \frac{|\mathbf{r}-\mathbf{r}'|}{v_s}\right). \tag{4}$$

The aforementioned equation describes a relationship in which the detected PA pressure at position $\mathbf{r}$ and time t comes from sources over a spherical surface centered at $\mathbf{r}$ with a radius of $|\mathbf{r}-\mathbf{r}'|$. For an inverse problem to (4), a reconstruction equation is derived for exact reconstruction of initial pressure distribution in an analytic reconstruction method such as UBP [10]. The only way to obtain the absorption distribution is to compensate light

fluence after the reconstruction of initial pressure distribution. This process also amplifies noise and artifacts, especially under limited-view conditions, resulting in a low-quality image.

In the proposed method, we separate the light fluence and the absorption coefficient at each voxel position. The absorption coefficients are estimated by a model-based method. We assume mean absorption and scattering coefficients for the background material. In this case, the light fluence distribution can be accurately obtained by a Monte Carlo method [33] after capturing incident light patterns. Another common approach for computing light fluence is to solve a photon diffusion equation using the finite element method [34], [35] at a high speed. However, the Monte Carlo solution can be greatly speed up using a high-performance parallel implementation.

Based on the (4), the forward model for calculating PA signals can be expressed in a matrix form as

$$\mathbf{p} = \mathbf{A}\Phi\boldsymbol{\mu}_a \tag{5}$$

where $\mathbf{A}$ denotes the system matrix representing the geometric relationship between the initial pressure and the detected PA signals, Φ is a diagonal matrix representing the light fluence, and $\mathbf{p}$ denotes the detected PA signals. The detailed form of $\mathbf{A}$ is

$$A_{i,j} = \frac{A'_{i,j+1} - A'_{i,j-1}}{2\Delta t} \tag{6}$$

where i is the index of sensor's position, j is the index of PA signal, Δt is the time interval between two sampling points, and $A'_{i,j}$ denotes the velocity potential. In the planar-measurement environment, the time of sound propagation through a voxel is longer than the sampling interval, and consequently the pressure data are not continuous after a finite-difference calculation. This process induces fluctuations with large amplitude, which prevent high-accuracy forward modeling. In this research, we assume voxel as sphere. The PA wave emitted from a small spherical source has a velocity potential profile of a Gaussian function [15], [36], [37] under the following assumption: the density distribution of absorbed energy in a sphere is a Gaussian distribution. The aforementioned assumption may lead to a problem that the accuracy of Gaussian interpolation is not very high. However, the advantage of Gaussian interpolation is that it can provide high-performance calculation. The imaging domain in this research is 3-D and large; hence, the system-matrix computation is time consuming. In order to achieve a good balance between calculation time and accuracy, the Gaussian kernel is chosen to interpolate the velocity potential data. The definition of the interpolated velocity potential item is

$$\begin{aligned} A'_{i,j} &= \frac{\beta}{4\pi C_p}\frac{h_{i,j}}{R_{i,j}} \\ R_{i,j} &= |\mathbf{r}_i - \mathbf{r}_j| \\ h_{i,j} &= \begin{cases} \exp\left(\frac{-2(R_{i,j}-t_j v_s)^2}{\Delta^2}\right) : \text{if} |t_j - \frac{R_{i,j}}{v_s}| < \Delta/v_s \\ 0 : \text{else} \end{cases} \end{aligned} \tag{7}$$

where Δ is the distance between the central points of adjacent voxels.

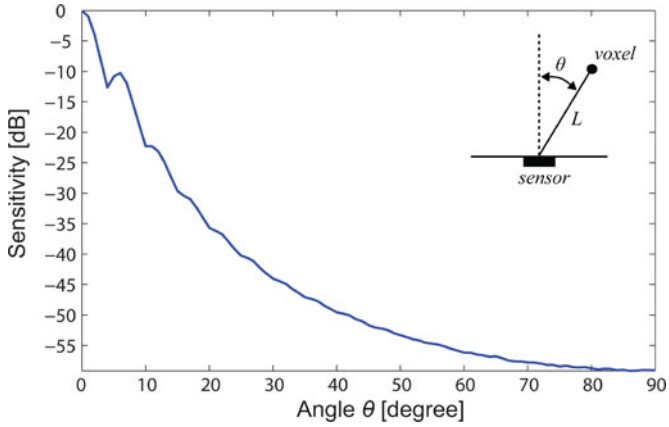

Fig. 1. Angular sensitivity of a 2×2 mm^2 unfocused rectangular transducer. The distance between transducer and target is $L = 10$ mm. The horizontal axis represents the wave incident angle θ (in degree), and the vertical axis represents the sensitivity of the transducer. The DREAM toolbox [38] was used to calculate the result.

The quantitative absorption distribution is estimated by minimizing the l_2 norm between the detected signals and the PA signals calculated by the forward model:

$$\boldsymbol{\mu}'_a = \arg\min_{\boldsymbol{\mu}_a} \|\mathbf{p}_\mathbf{d} - \mathbf{A}\Phi\boldsymbol{\mu}_a\|_2. \tag{8}$$

Here, $\mathbf{p}_\mathbf{d}$ represents the detected PA signals, and $\boldsymbol{\mu}'_a$ is the optimal estimation of the absorption coefficient distribution. The conjugate gradient (CG) method is used to find the optimal estimation.

B. Matrix Compression

Although model-based reconstruction for PAT has many advantages, it has a critical limitation that the system matrix consumes huge amounts of memory without matrix compression. In order to apply the proposed method to clinical situations, we developed matrix-compression methods to reduce the memory requirement. First, matrix $\mathbf{A}$ is a sparse matrix in which more than 99% of the entries are zero. The required memory can be greatly reduced by using the compressed sparse row (CSR) format [40], where nonzero entries are stored in continuous memory locations and corresponding column indices are stored in an integer array. We use another integer array to store the index of first nonzero entry in each row.

In PAT, the ultrasound transducer is generally assumed to detect pressure waves in directions from 0° to 90° with the same sensitivity; however, in real situations the sensitivity is not uniform due to the finite-sized unfocused transducer. The spatial impulse response (SIR) of the transducer introduces limited detection angles, waveform distortion, and time-delay errors for reconstruction [22], [23]. For example, the angular sensitivity of a 2×2 mm^2 unfocused rectangular transducer is plotted in Fig. 1. When the incident angle is 45°, the sensitivity is -50 dB, which is less than the detectable signal level for a conventional sensor. Hence, the incident wave can be ignored. In order to compress the matrix $\mathbf{A}$, if the incident angle exceeds a given threshold, its value is set to zero so that the entry is not stored.

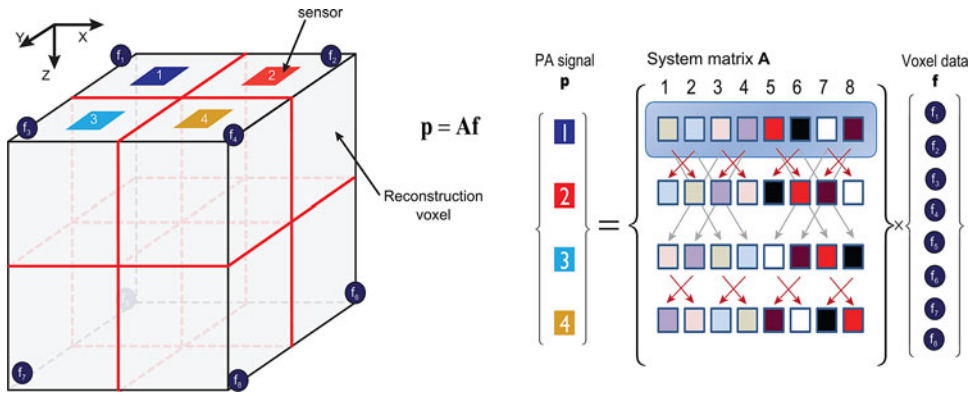

Fig. 2. Matrix compression using the symmetry of wave propagation. For simplicity, in this figure only four sensors and eight voxels are illustrated. Only the first 1/4 row of $\mathbf{A}$ is stored; coefficients in other rows can be obtained by rearranging the order of the first 1/4 row's coefficients.

With this approach, matrix $\mathbf{A}$ can be further decreased to about half its original size when the threshold value is 45°.

The matrix can be further compressed to one-fourth its original size based on the symmetry of wave propagation [21], as illustrated in Fig. 2. This figure depicts only four sensors and eight voxels. The PA signals detected by sensor 1 are calculated from the inner product $\mathbf{A}(\mathbf{1},:)\cdot\mathbf{f}$. Because sensors 2 and 1 are symmetrical about the Y-axis, the second row of $\mathbf{A}$ can be obtained by changing the X-axis order of the first row. Similarly, the third row of $\mathbf{A}$ can be obtained by changing the Y-axis order of the first row, and the fourth row of $\mathbf{A}$ can be obtained by changing the X- and Y-axis orders of the first row. Therefore, only one-fourth of the rows of $\mathbf{A}$ are necessary for reconstruction, and other rows' data can be obtained during the multiplication of sparse matrix and vector. In total, the required memory can be reduced to approximately 1/250 its original size by using the aforementioned methods.

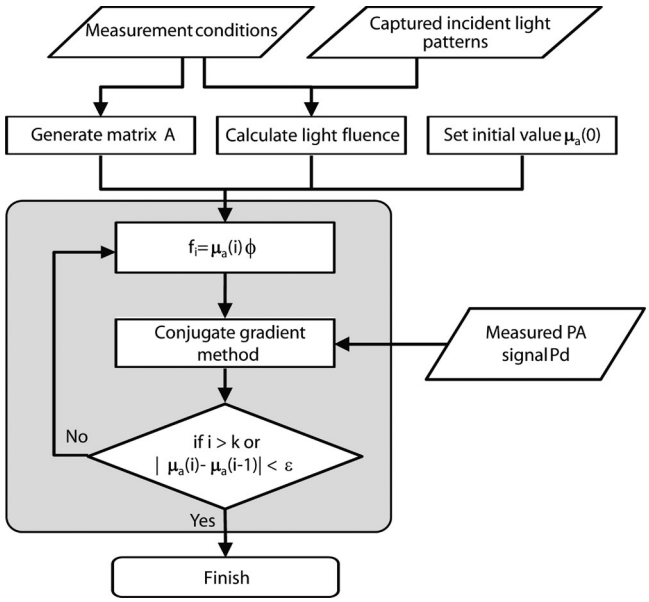

Fig. 3. Flow-chart of the proposed method.

C. Implementation

The flow-chart of the proposed method is presented in Fig. 3. After the measurement conditions are determined, the system matrix $\mathbf{A}$ is calculated according to the geometry parameters. The incident light patterns are captured by a camera, and the distribution of light fluence is then calculated using the Monte Carlo method, where the previously estimated mean absorption and reduced scattering coefficients for the background material are used. The initial values of $\boldsymbol{\mu}_a(i)$ are set to zeros or UBP reconstructed values. Next, the reconstruction is performed, and the CG method is adopted to solve the optimization problem. In each CG iteration, the residual is computed by using the precalculated absorbed energy $\mathbf{f}_i$, while the value is updated to the $\boldsymbol{\mu}_a(i)$. This differs slightly from the traditional CG method, because using the updated absorption coefficients to calculate the residual at each iteration leads to divergence, which prevents convergence to the true value. In our experiments, the optimal number of iterations in the inner CG is 5 to 8. At the outer iteration, computation is terminated when the iteration loop number exceeds a given number or the change of absorption coefficients is less than a threshold.

III. Simulation and Phantom Experiments

A. Numerical Simulation

The proposed method was evaluated by numerically simulating a hypothetical model, as illustrated in Fig. 4. In this model, five wire targets with a diameter of 0.5 mm embedded in a uniform block ($32\times32\times32$ mm^3) were simulated as shown in Fig. 4(a). The simulation parameters are summarized in Table I. The background's absorption coefficient was $\mu_a = 0.078\,\text{cm}^{-1}$, and its reduced scattering coefficient was $\mu_s' = 9.306\,\text{cm}^{-1}$. The absorption coefficient of the wire target was $\mu_a = 4.3\ \text{cm}^{-1}$. Forward illumination (toward the probe) was used as illustrated by Fig. 4(a), and the incident light pattern is shown in Fig. 4(b), which adopts data captured by a camera as well as phantom experiment.

The light fluence was calculated by the Monte Carlo method using the incident light pattern and the mean absorption and scattering coefficients of the background. Fig. 4(c) shows the 3-D distribution of light fluence (left), light fluence distribution

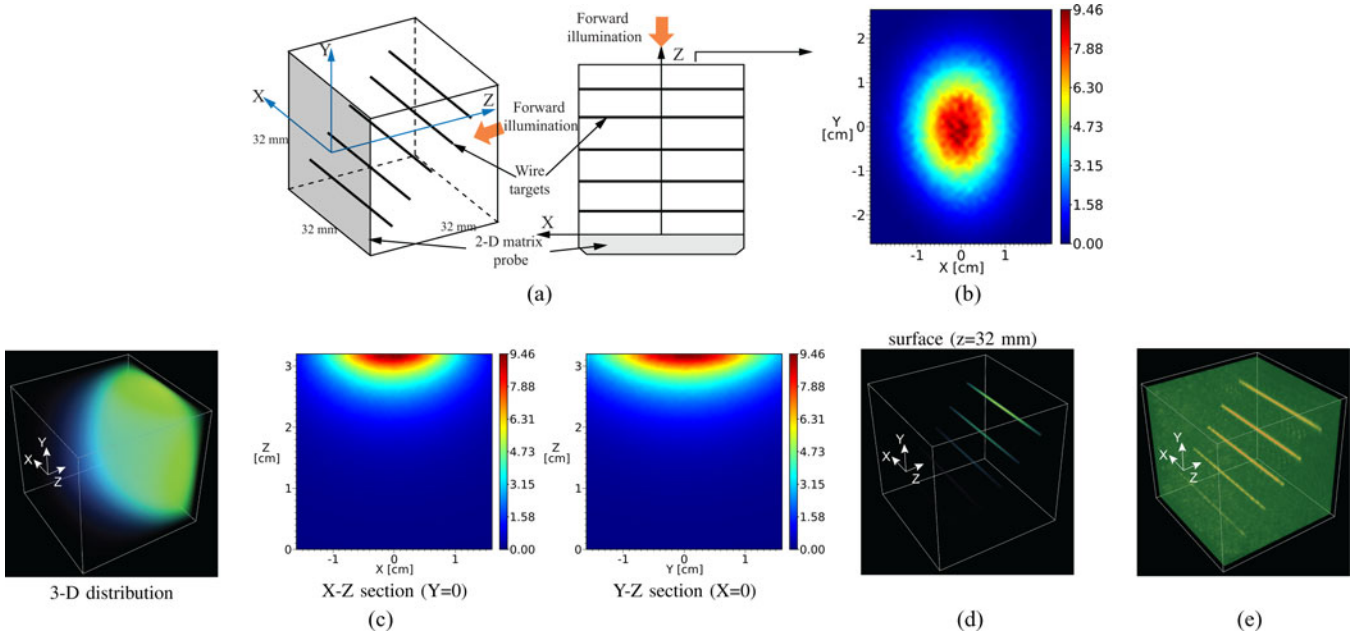

Fig. 4. Numerical simulation model. (a) Alignment of wire targets as optical absorber, ultrasound probe, and optical source. (b) Incident light pattern on the surface ($z = 32$ mm) by forward illumination. (c) Light fluence distribution calculated by the Monte Carlo method; 3-D distribution (Left), cross section of *X*–*Z* plane at $Y = 0$ (middle), *Y*–*Z* plane at $X = 0$ (right). (d) Initial pressure distribution. (e) Absorption distribution reconstructed by the proposed method.

TABLE I
SIMULATION PARAMETERS

Parameter name	Value
Sound speed	1500 m/s
Sampling frequency	20 MHz
Sampling point number	750
Sensor number in x and y axes	16
Sensor pitch in x and y axes	2.0 mm
Voxel number in x, y, and z axes	64
Voxel size in x, y, and z axes	0.5 mm

on the cross section of *X*–*Z* plane at $y = 0$ (middle), and *Y*–*Z* plane at $x = 0$ (right). The PA waves were simulated using (4), and -30-dB white noise was added. Fig. 4(d) shows the 3-D distribution of initial pressure. Finally, the 3-D absorption distribution reconstructed by the proposed method is shown in Fig. 4(e).

All programs were implemented in parallel and run on a cluster system containing six workstations. Each workstation had two quad-core Xeon 2.4-GHz CPUs. The floating point operation per second (FLOPS) of the cluster system was 251 G. It took 42 s to calculate the light fluence distribution. After the simulated PA signals were obtained, the reconstruction program was used to reconstruct the absorption distribution. The required memory of matrix $\mathbf{A}$ before compression was 402.653 GB; after compression it was reduced to 1.255 GB. The calculation time for one iteration was 0.6 s, and there were 400 iterations in total.

Fig. 5 presents the maximum intensity projection (MIP) images reconstructed by the proposed method, compared with the conventional quantitative reconstruction method, that is, UBP with fluence compensation after reconstruction. Here, MIP *X*–*Y* (top images) is the projection along the *Z*-axis, MIP *X*–*Z* (middle images) is the projection along the *Y*-axis, and MIP *Z*–*Y* (bottom image) is the projection along the *X*-axis.

Fig. 5(a) presents MIP images of the given absorption distribution. Fig. 5(b) presents MIP images of the absorbed optical energy distribution. The resulting MIP images in Fig. 5(c) show the absorption distribution reconstructed by the conventional method. The images reconstructed by the proposed method are presented in Fig. 5(d). The profiles along the Z-direction at $x = 0$ in MIP *X*–*Z* are presented in Fig. 5(e). The unit of absorbed optical energy images is mJ/cm^3, and the unit of absorption coefficient is cm^{-1}.

In the conventional method, the initial pressure is first reconstructed by the UBP method, and then the absorption coefficient is obtained by dividing the light fluence. The light fluence decreases rapidly in tissue, and hence the light fluence is low at the deep location. In the simulation, -30-dB white noise was added into the PA signals, and consequently noise and artifacts were produced in the UBP reconstruction. The noise and artifacts are amplified in low fluence regions after conventional fluence compensation. In contrast, these are greatly reduced by the proposed method. From the profiles, we can see that the CNR of the target at $z = 16$ mm is 6.46 for the proposed method and 1.39 for the conventional method. The CNR improvement is 4.63 times.

B. Phantom Experiment

Performances were also evaluated by a tissue-mimicking phantom with embedded absorbers as illustrated in Fig. 6(a). The base of the tissue-mimicking phantom with a size of 70 (X) $\times$ 120 (Y) $\times$ 50 (Z) mm^3 was made with urethane gel and curing agent. The speed of sound in the base phantom was 1391 m/s. Rubber wires with 0.3 mm diameter were embedded in the base phantom. The absorption and reduced scattering coefficients of the base phantom were 0.078 and 9.306 cm^{-1} at a wavelength of 797 nm. We utilized a spectrophotometer to measure the

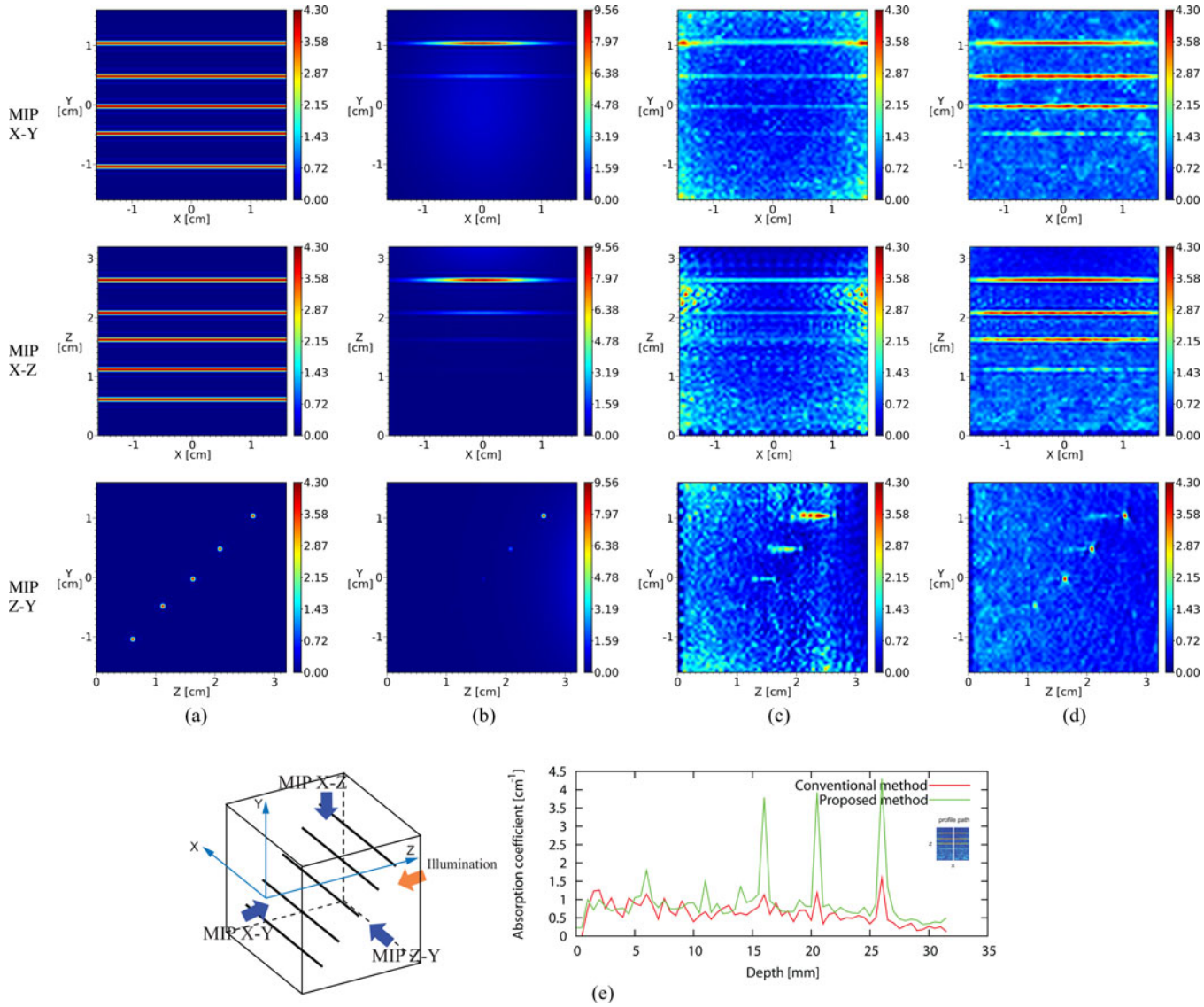

Fig. 5. Simulation model and images reconstructed by the proposed method and the conventional quantitative reconstruction method. Each depicts the MIP image. (a) Simulation model: given absorption distribution. (b) Absorbed optical energy distribution. (c) Resulting images of absorption coefficient reconstructed by the conventional quantitative reconstruction method. (d) Resulting images of absorption coefficient reconstructed by the proposed method. (e) Profiles along the Z-direction at $x = 0$ in MIP X–Z.

reflection and transmission properties of the phantom sample. An iterative method was adopted to estimate the optimal optical properties of the sample. First, initial optical parameters were selected. At each iteration, the Monte Carlo method was used to calculate the reflection and transmission values, and the Newton method was used to update the estimated optical parameters. The iteration was terminated when the differences between measured and calculated values of reflection and transmission were less than a threshold. The last estimated values were regarded as the optimal absorption and reduced scattering coefficients of the sample.

A PA imaging system with dual illumination [39] was utilized in the phantom experiment, where dual lasers illuminate the target so that it is possible to image deeper regions in tissues. Two sets of a Ti:Sa laser (LT-2211, LOTIS TII) pumped by a Q-switched Nd:YAG laser (LS-2137, LOTIS TII) were adopted as the excitation source to provide 15-ns laser pulses with a 10-Hz pulse repetition rate. One laser was used for backward illumination (probe side), and the other for the forward direction (opposite side from the probe), as illustrated in Fig. 6(a). A wavelength of 797 nm was adopted in this experiment. The maximum incident light energy densities from backward and forward illumination on the sample surface were 3.48 and 9.46 mJ/cm^2, respectively. The distributions of incident light energy density captured by a camera are given in Fig. 6(b) and (c), where the unit of the colorbar is mJ/cm^2. The light fluence was calculated by the Monte Carlo method, as shown in Fig. 6(d). The profile of light fluence at the center of the probe along the depth direction is plotted in Fig. 6(e).

A 2-D 345-element [15 (X) $\times$ 23 (Y)] matrix probe with element size of 2×2 mm^2 was used in our system. The rectangular shape of the matrix probe enables direct illumination of tissue

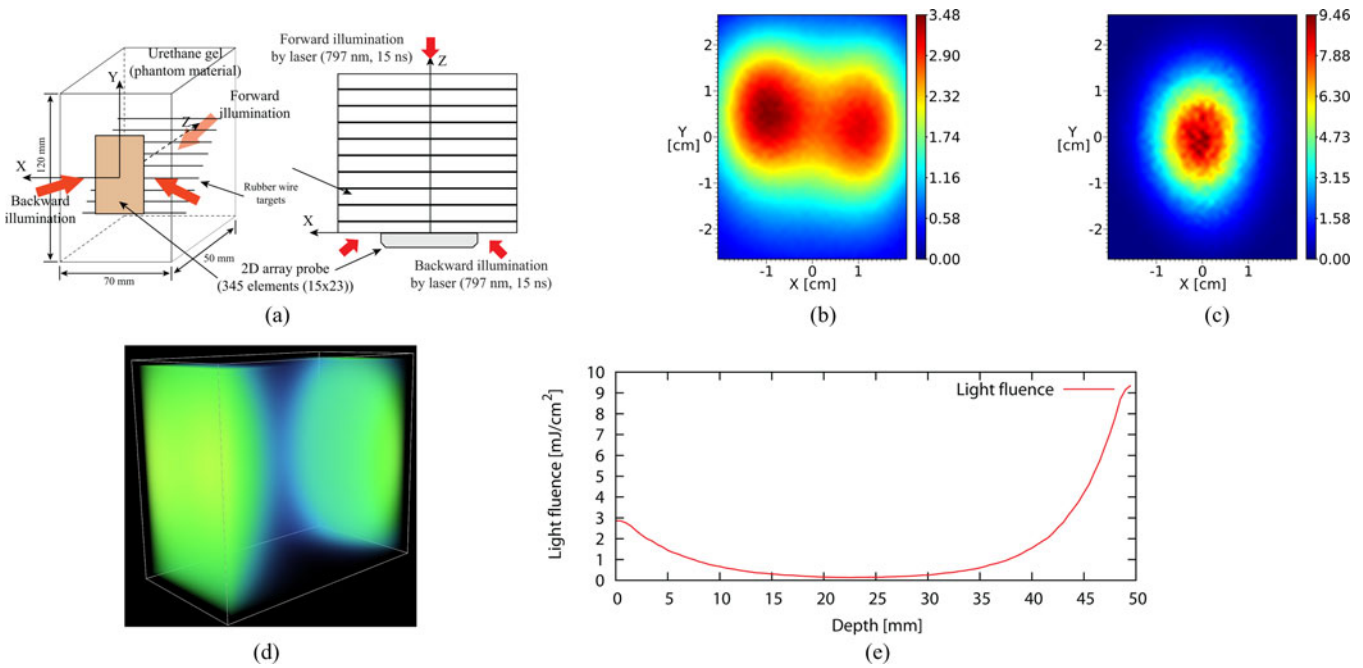

Fig. 6. Configuration of phantom experiment. (a) Phantom and settings of probe and optical source. (b) Incident light pattern (light energy density distribution) on the back side (probe side); the unit of the colorbar is mJ/cm^2. (c) Incident light pattern on the forward side (opposite side from probe); the unit of the colorbar is mJ/cm^2. (d) Light fluence calculated by the Monte Carlo method. (e) Profile of light fluence at the center of the probe along the depth direction.

surfaces in front of the array transducer through a 10-mm thick holding plate. The transducer frequency was designed to be 1 MHz with a bandwidth greater than 70%. The array had a detection area of 30 $\times$ 46 mm^2. Custom-made front-end electronics and a data-acquisition system were employed to obtain PA signals for image reconstruction. The front-end electronics consist of 345-channel receivers. We adopted a fixed amplifier gain of 40 dB, a sampling rate of 20 MHz, and 1280 sampling points. The received PA signals were amplified, filtered, and digitized in the data-acquisition system. The digitized PA signals were transferred to a PC for further signal processing and image reconstruction. In the reconstruction, the voxel size was set to 0.5 mm for all axes, and the reconstruction range was 28 (X) $\times$ 44 (Y) $\times$ 50 (Z) mm^3.

The images were reconstructed on the same cluster system as described in Section III-A. It took 65 seconds to calculate the light fluence distribution. In order to obtain the best performance, only PA signals from 14 $\times$ 22 channels were used, although the matrix probe has 15 $\times$ 23 channels. The required memory for the matrix $\mathbf{A}$ before compression was 1.554 TB; after compression, the size was reduced to 6.250 GB. The calculation time for one iteration was 1.2 seconds, and there were 240 iterations in total.

The resulting images are presented in Fig. 7. Fig. 7(a) and (b) presents MIP images reconstructed by the UBP method without and with fluence compensation, respectively. The MIP images reconstructed by the proposed method are presented in Fig. 7(c). The profiles along the Z-direction at $x = 0$ in MIP X–Z are plotted in Fig. 8.

In the resulting images, the display is in an arbitrary unit. In this research, the absolute values of absorption coefficient can be reconstructed in theory, but are actually difficult to calculate for the following reasons. 1) The attenuation of ultrasound wave is not considered, and the Grüneisen coefficients are assumed constant in the whole region. 2) In our experiment, it is difficult to measure the absorption coefficient of rubber wires. Therefore, it is difficult to normalize the reconstructed value to the absolute value. On the other hand, the main objective of our research is to image macroscopic capillary vessel density; therefore, the absolute value of absorption coefficient is not very necessary. As a result, the reconstructed images of the phantom experiment are displayed in an arbitrary unit.

The resulting images indicate that the absorption distribution reconstructed using the proposed method is better than that using the conventional fluence compensation method. The light fluence around $z = 25$ mm is low. In this case, the wire target at the position can hardly be seen in the resulting imaging reconstructed by the UBP without fluence compensation, and much noise and artifacts appear in the resulting images reconstructed by the conventional fluence compensation method. We compared the proposed method to the UBP with and without fluence compensation, and the evaluation parameters include mean and standard deviation of targets' absorption coefficients, and average CNR. The mean and standard deviation are 0.458 and 0.275 in the UBP without fluence compenation, 0.482 and 0.169 in the UBP with fluence compensation. Our method improved the two values to 0.624 and 0.145. The average CNR is 4.19 in the UBP with fluence compensation, and in the proposed method it is 4.84 with an improvement of 15.51%. However, we also found that the average CNR in the UBP without light fluence is 11.79, and either of fluence compensation methods yields lower values than it. The reason that CNR becomes low is that noise and artifacts amplification cannot be avoided during the fluence compensation. But in the proposed method, we

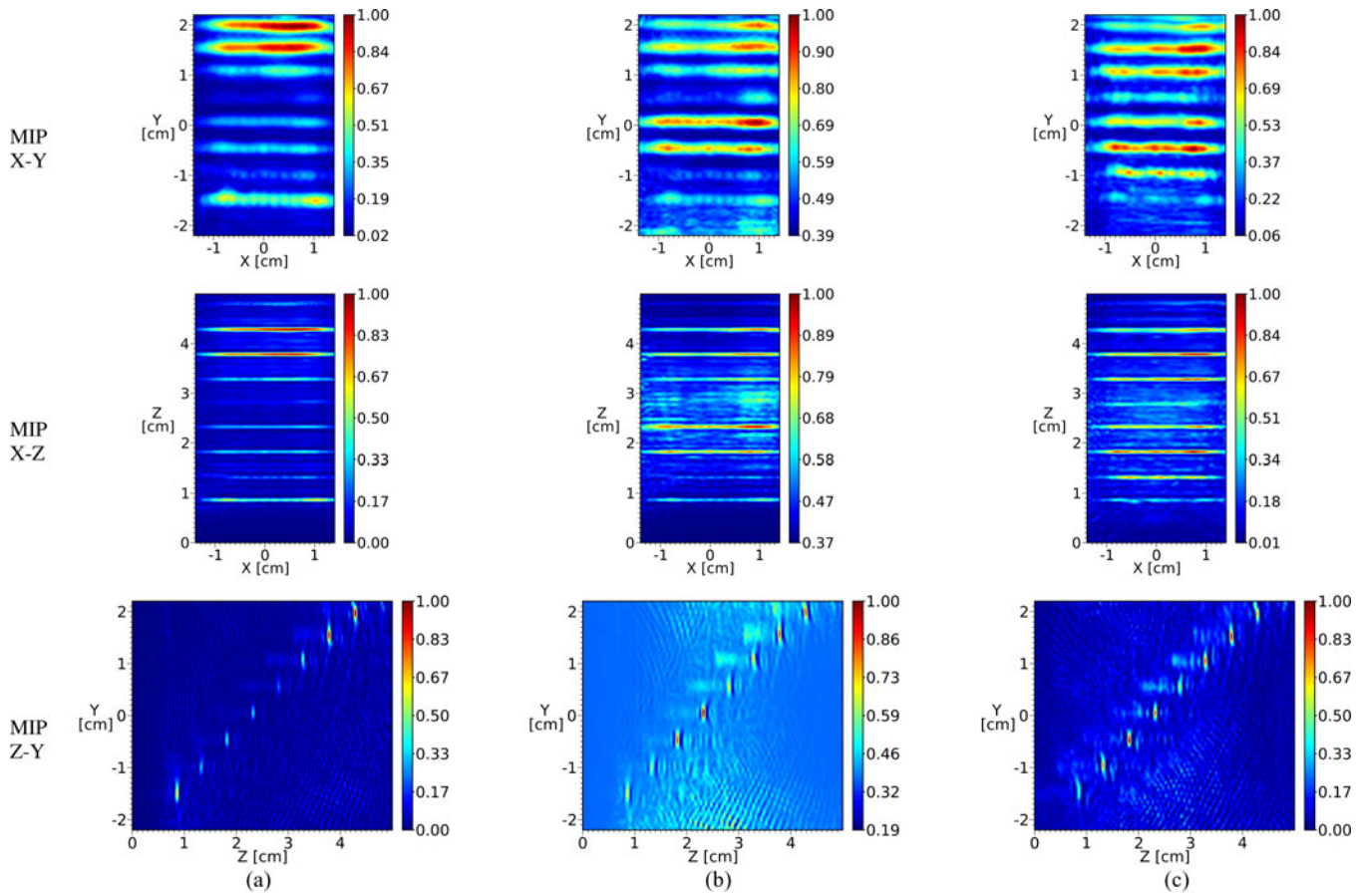

Fig. 7. Results of image reconstructed from experiment data. (a) Images reconstructed by the UBP method without fluence compensation. (b) Images reconstructed by the UBP method with conventional fluence compensation. (c) Images reconstructed by the proposed method.

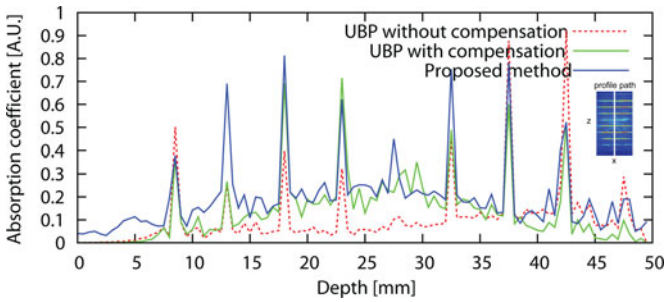

Fig. 8. Profile along Z direction at $X = 0$ in MIP X–Z.

improved the process of fluence compensation, which minimizes the overall noise and artifacts. As a result, the amplification of noise and artifacts is suppressed, and the CNR exceeds that of conventional fluence compensation method. Although the UBP without fluence compensation outperforms either of the fluence compensation methods on the CNR, the quantitative absorption coefficients are no better than them. Therefore, the proposed method achieves a better balance between CNR and quantitative reconstruction.

In addition, because the imaging region is 3-D and furthermore with a large region, which leads to extremely low values of light fluence in some local regions, the absorbed energy in these local regions is low and hence the initial pressure is low. Our system also suffers from the hardware limitations on enhancing the sensitivity of ultrasound transducer and the SNR of ADC. Based on the aforementioned two points, it becomes difficult to obtain accurate reconstruction at low fluence regions.

IV. Discussion

In this study, we assume mean absorption and reduced scattering coefficients for the background material. The light fluence distribution is calculated by the Monte Carlo method [33], using the assumed mean absorption and scattering coefficients, and captured incident light patterns. Fluence compensation and reconstruction are combined in order to achieve better performance. In the current research stage, although light fluence is calculated only once using the estimated mean absorption and reduced scattering coefficients for the background material, the proposed method has the capability to update the light fluence at each iteration using the newly estimated absorption coefficient [24]. In our method, it is important to exactly calculate the light fluence distribution for better reconstruction under the assumption of mean optical parameters are known. There exist several solutions that can overcome the restriction of optical inhomogeneity. First, a diffuse optical tomography (DOT) [41], [42] can be used to estimate the low-resolution absorption distribution so as to assist the light fluence calculation. Second, not only absorption distribution but also Grüneisen

distribution can be estimated in the multi-illumination method proposed by Zemp *et al*. [29], [30]. These methods have the potential to provide robust and accurate light fluence distribution for planar-scanning schemes.

In addition, for reducing memory requirements and accelerating reconstruction speed, we developed matrix-compression methods. The system matrix was losslessly compressed by using the CSR format and storing only one-fourth of the rows based on the symmetry of wave propagation, and further compressed with little loss based on the nonuniform angular sensitivity of ultrasound transducer. As a result, the memory required by the matrix could be effectively reduced, and the reconstruction speed was also improved. Our method achieves a better balance between memory size and computation time. Moreover, these compression methods can be applied to not only planar measurement environment but also cylindrical and spherical measurement environments. Additionally, our approach will naturally benefit from integrating compressed sensing methods [28], [46], [47]. A GPU accelerated [48] compressed sensing reconstruction method can also be expected to boost the calculation speed, because our method has the potential of high-performance parallel computation.

Although our proposed method can output better images, the artifacts are still distinct. Some limitations need to be resolved in order to obtain high-quality reconstruction images.

It affects the quality of PAT reconstruction how to compensate transducer properties, i.e., SIR related with element geometry and electromechanical response. Regarding element geometry, it was used to generate PAT signals based on a forward model. However, direct compensation of these transducer properties is not provided in this paper. We attempted to incorporate the compensation of SIR as the geometry of elements into the system matrix. In the simulation, SIR compensation achieved a significant improvement in the lateral resolution, while it did not demonstrate effective results in phantom experiment. We also conducted deconvolution techniques to compensate received PA signals by using the measured transducer's impulse response. However, the reconstructed images did not have distinct improvement. The main reason is that the central frequency (1 MHz) and bandwidth (70%) of the matrix probe are low, and consequently, the noise was not effectively suppressed. In the next study, a more effective deconvolution method and SIR compensation for transducer with wide bandwidth will be explored.

The model-based method basically requires a large amount of memory even if matrix compression is used. In some cases, this may be a limitation to the practical use of the model-based method. If the system matrix is explicitly stored, the memory complexity is approximately $O(n^3 n_x n_y n_s)$, where n is proportional to the voxel number in one side of the reconstruction region, n_x and n_y are the captured data in *X*- and *Y*-direction, respectively, and n_s is the sampling point number. If the system matrix is implicitly implemented, the computation time is not acceptable. Hence, the model-based method is hardly suitable to high-resolution PAT reconstruction. For example, when fine temporal sampling of high-frequency PA signals or wide area measuring with a small spatial sampling interval are required in order to avoid aliasing artifact [2], the system matrix size is apt to be larger than the computer's memory size. Hence, the model-based method is hardly suitable to the high resolution and large area PAT reconstruction. On the other hand, for our developed PA mammography (PAM) system, the objective is to provide an imaging tool for early breast cancer diagnosis based on the capillary vessel density of cancer. The spatial resolution of PAM is significantly restricted because of ultrasound attenuation caused by a large reconstruction range. Therefore, PAM is used to provide macroscopic vessel density instead of microscopic distribution. The results showed the proposed method attained enough spatial resolution to detect 0.3-mm wire targets, which is useful for our PAM system.

This study uses the CG method to solve the optimization problem, but in some cases this method converges to local minima. Therefore, regularization methods are usually adopted for computing a stable solution. We have investigated various penalty functions such as compressed sensing methods (e.g. L1–LS solver). When the problem size is small, the expected fast convergence rate and satisfactory reconstruction can be achieved. When the problem size increases, however, the convergence rate declines rapidly, and even an acceptable optimization result cannot be obtained. If nonlinear optimization methods are used, it is impossible to calculate the Jacobi matrix in a common computer. In this research, we confirmed that the CG method finally converges to the same solution for different initial values. In the future work, we will continue to research a better optimization method for solving the large-scale optimization problem.

Besides the aforementioned limitations, the sound speed heterogeneity also needs to be considered to improve the image quality. In other studies [18], [43]–[45], the sound speed heterogeneity can be resolved by compensating the sound speed during the reconstruction. In subsequent studies, an effective sound speed estimation method especially suitable for planar scanning PAT will be researched, and better reconstruction results are expected.

V. Conclusion

In this paper, we presented a fluence-compensation and reconstruction method for 3-D planar PAT. Light fluence compensation performed at each iteration, which minimizes the amplification of noise and artifacts. Furthermore, matrix compression methods made the proposed method applicable to 3-D reconstruction under planar measurement conditions, and the calculation speed was also accelerated. The simulation and phantom experiment results indicated that the proposed method reconstructs better quality images. We expect that the capability of increasing imaging depth will broaden clinical applications of PAT.

Acknowledgment

The authors would like to thank the anonymous reviewers for their valuable comments to improve this paper. The authors would also like to thank T. Nakajima and R. Nanaumi for helping to evaluate the optical properties of the phantom, and the team members of the Medical Imaging Project in Canon Inc. for the PA imaging system development.

REFERENCES

[1] C. Li and L. V. Wang, "Photoacoustic tomography and sensing in biomedicine," *Phys. Med. Biol.*, vol. 54, no. 19, pp. R59–R97, 2009.

[2] M. Xu and L. V. Wang, "Photoacoustic imaging in biomedicine," *Rev. Sci. Instrum.*, vol. 77, p. 041101, 2006.

[3] L. V. Wang and H.-i Wu, *Biomedical Optics: Principles and Imaging*. New York: Wiley, 2007.

[4] C. G. A. Hoelen and F. F. M. de Mul, "Image reconstruction for photoacoustic scanning of tissue structures," *Appl. Opt.*, vol. 39, no. 31, pp. 5872–5883, 2000.

[5] C. K. Liao, M. L. Li, and P. C. Li, "Optoacoustic imaging with improved synthetic focusing," *Proc. SPIE*, vol. 5697, pp. 255–262, 2005.

[6] S. Park, A. B. Karpiouk, S. R. Aglyamov, and S. Y. Emelianov, "Adaptive beamforming for photoacoustic imaging using linear array transducer," in *Proc. IEEE Ultrason. Symp.*, 2008, pp. 1088–1091.

[7] R. A. Kurger, P. Liu, Y. R. Fang, and C. R. Appledorn, "Photoacoustic ultrasound (PAUS)—Reconstruction tomography," *Med. Phys.*, vol. 22, no. 10, pp. 1605–1609, Oct. 1995.

[8] R. A. Kruger, D. R. Reinecke, and G. A. Kruger, "Thermoacoustic computed tomography—Technical considerations," *Med. Phys.*, vol. 26, no. 9, pp. 1832–1839, Sep. 1999.

[9] S. R. Deans, "The Randon transform and some of its applications," New York: Wiley.

[10] M. Xu and L. V. Wang, "Universal back-projection algorithm for photoacoustic computed tomography," *Phys. Rev. E*, vol. 71, no. 1, p. 016706, 2005.

[11] M. Xu and L. V. Wang, "Time-domain reconstruction for thermoacoustic tomography in a spherical geometry," *IEEE Trans. Med. Imag.*, vol. 21, no. 7, pp. 814–822, Jul. 2002.

[12] K. P. Kostli, D. Frauchiger, J. J. Niederhauser, G. Paltauf, H. P. Weber, and M. Frenz, "Optoacoustic imaging using a three-dimensional reconstruction algorithm," *IEEE J. Sel. Top. Quantum Electron.*, vol. 7, no. 6, pp. 918–923, Nov. 2001.

[13] Y. Xu, D. Feng, and L. V. Wang, "Extract frequency-domain reconstruction for thermoacoustic tomography—I: Planar geometry," *IEEE Trans. Med. Imag.*, vol. 21, no. 7, pp. 823–828, Jul. 2002.

[14] Y. Xu, D. Feng, and L. V. Wang, "Extract frequency-domain reconstruction for thermoacoustic tomography—II: Cylindrical geometry," *IEEE Trans. Med. Imag.*, vol. 21, no. 7, pp. 829–833, Jul. 2002.

[15] G. Paltauf, J. A. Viator, S. A. Prahl, and S. L. Jacques, "Iterative reconstruction algorithm for optoacoustic imaging," *J. Acoust. Soc. Amer.*, vol. 112, no. 4, pp. 1536–1544, 2002.

[16] J. Zhang, M. A. Anastasio, P. J. L. Riviere, and L. V. Wang, "Effects of different imaging models on least-squares image reconstruction accuracy in photoacoustic tomography," *IEEE. Trans. Med. Imag.*, vol. 28, no. 11, pp. 1781–1790, Nov. 2009.

[17] S. Ma, S. Yang, and H. Guo, "Limited-view photoacoustic imaging based on linear-array detection and filtered mean-backprojection-iterative reconstruction," *J. Appl. Phy.*, vol. 106, p. 123104, 2009.

[18] Z. Jing, W. Kun, Y. Yongyi, and A. A. Mark, "Simultaneous reconstruction of speed-of-sound and optical absorption properties in photoacoustic tomography via a time-domain iterative algorithm," *Proc. SPIE*, vol. 6856, p. 68561, 2008.

[19] A. Rosenthal, D. Razansky, and V. Ntziachristos, "Fast semi-analytical model-based acoustic inversion for quantitative optoacoustic tomography," *IEEE Trans. Med. Imag.*, vol. 29, no. 6, pp. 1275–1285, Jun. 2010.

[20] S. Bu, K. Kondo, M. Yamakawa, T. Shiina, K. Fukutani, Y. Someda, and Y. Asao, "Adaptive and quantitative reconstruction algorithm for photoacoustic tomography," in *Proc. SPIE*, vol. 7899, p. 78992G, 2011.

[21] K. Tanji, K. Watanabe, K. Fukutani, Y. Asao, T. Yagi, M. Yamakawa, and T. Shiina, "Advanced model-based reconstruction algorithm for practical three-dimensional photoacoustic imaging," in *Proc. SPIE*, vol. 7899, p. 78992K, 2011.

[22] M. L. Li, Y. C. Tseng, and C. C. Cheng, "Model-based correction of finite aperture effect in photoacoustic tomography," *Opt. Express*, vol. 18, no. 25, pp. 26285–26292, 2010.

[23] K. Wang, S. A. Ermilov, R. Su, H. P. Brecht, A. A. Oraevsky, and M. A. Anastasio, "An imaging model incorporating ultrasonic transducer properties for three-dimensional optoacoustic tomography," *IEEE Trans. Med. Imag.*, vol. 30, no. 2, pp. 203–214, Feb. 2011.

[24] B. T. Cox, S. R. Arridge, K. P. Kostli, and P. C. Beard, "Two-dimensional quantitative photoacoustic image reconstruction of absorption distribution in scattering media by use of a simple iterative method," *Appl. Opt.*, vol. 45, no. 8, pp. 1866–1875, 2006.

[25] Z. Yuan, Q. Wang, and H. Jiang, "Reconstruction of optical absorption coefficient maps of heterogeneous media by photoacoustic tomography coupled with diffusion equation based regularized Newton method," *Opt. Express*, vol. 15, no. 26, p. 18076, 2007.

[26] B. T. Cox, S. R. Arridge, and P. C. Beard, "Estimating chromophore distribution from multiwavelength photoacoustic images," *J. Opt. Soc. Amer.*, vol. 26, no. 2, p. 443, 2009.

[27] A. Rosenthal, D. Razansky, and V. Ntziachristos, "Quantitative optoacoustic signal extraction using sparse signal representation," *IEEE Trans. Med. Imag.*, vol. 28, no. 12, pp. 1997–2006, Dec. 2009.

[28] A. Rosenthal, D. Razansky, and V. Ntziachristos, "Sparse signal representation at the service of quantitative optoacoustic tomography," in *Proc. SPIE*, vol. 7564, p. 75640S, 2010.

[29] R. J. Zemp, "Quantitative photoacoustic tomography with multiple optical sources," *Appl. Opt.*, vol. 49, no. 18, p. 3566, 2010.

[30] P. Shao, B. Cox, and R. J. Zemp, "Estimating optical absorption, scattering, and Grueneisen distributions with multi-illumination photoacoustic tomography," *Appl. Opt.*, vol. 50, no. 19, p. 3145, 2011.

[31] P. M. Morse and K. U. Ingard, *Theoretical Acoustics*. Princeton, NJ: Princeton Univ. Press, 1987.

[32] G. J. Diebold, T. Sun, and M. I. Khan, "Photoacoustic monopole radiation in one, two, and three dimensions," *Phys. Rev. Lett.*, vol. 67, no. 24, pp. 3384–3387, 1991.

[33] L. H. Wang, S. L. Jacques, and L. Q. Zheng, "MCML - Monte Carlo modeling of photon transport in multi-layered tissues," *Comput. Methods Programs Biomed.*, vol. 47, pp. 131–146, 1995.

[34] S.R. Arridge, "Optical tomography in medical imaging," *Inverse Problems*, vol. 15, no. 2, p. R41, 1999.

[35] K. D. Paulsen and H. Jiang, "Spatially-varing optical property reconstruction using a finite element diffusion equation approximation," *Med. Phys.*, vol. 22, no. 6, pp. 619–701, 1995.

[36] C. G. A. Hoelen and F. F. M de Mul, "A new theoretical approach to photoacoustic signal generation," *J. Acoust. Soc. Amer.* vol. 106, no. 2, pp. 695–706 1999.

[37] M. W. Sigrist and F. K. Kneubuhl, "Laser generated stress waves in liquids," *J. Acoust. Soc. Amer.* vol. 64, pp. 1652–1663, 1978.

[38] B. Piwakowski and K. Sbai, "A new approach to calculate the field radiated from arbitrarily structured transducer array," *IEEE Trans. Ultra. Ferr. Freq. Con.*, vol. 46, no. 2, pp. 422–440, Mar. 1999.

[39] K. Fukutani, Y. Someda, M. Taku, Y. Asao, S. Kobayashi, T. Yagi, M. Yamakawa, T. Shiina, T. Sugie, and M. Toi, "Characterization of photoacoustic tomography system with dual illumination modes," in *Proc. SPIE*, 2011, vol. 7899, p. 78992J.

[40] E. F. D. Azevedo, M. R. Fahey, and R. T. Mills, "Vectorized sparse matrix multiply for compressed row storage format," in *Proc. Int. Conf. Comput. Sci.*, 2005, vol. 3514, pp. 99–106.

[41] A. Q. Bauer, R. E. Nothdurft, C. Li, L. V. Wang, and J. P. Culver, "Correcting for heterogeneous fluence profiles in photoacoustic imaging with diffuse optical tomography," presented at the Biomed. Opt., Miami, FL, 2010.

[42] C. Xu, P. D. Kumavor, A. Aguirre, and Q. Zhu, "Investigation of DOT-assisted photoacoustic tomography in reflection geometry," in *Proc. SPIE*, vol. 7899, p. 78990U, 2011.

[43] M. A. Anastasio, J. Zhang, X. Pan, Y. Zhou, G. Ku, and L. V. Wang, "Half-time image reconstruction in thermoacoustic tomography," *IEEE. Trans. Med. Imag.*, vol. 24, no. 2, pp. 199–210, Feb. 2005.

[44] H. Jiang, Z. Yuan, and X. Gu, "Spatially varying optical and acoustic property reconstruction using finite-element-based photoacoustic tomography," *J. Opt. Amer. A*, vol. 23, no. 4, pp. 878–888, 2006.

[45] J. Jose, R. G. H. Willemink, S. Resink, D. Piras, J. C. G. van Hespen, C. H. Slump, W. Steenbergen, T. G. van Leeuwen, and S. Manohar, "Passive element enriched photoacoustic computed tomography (PER PACT) for simultaneous imaging of acoustic propagation properties and light absorption," *Opt. Express*, vol. 19, no. 3, pp. 2093–2104, 2011.

[46] J. Provost and F. Lesage, "The application of compressed sensing for photo-acoustic tomography," *IEEE. Trans. Med. Imaging*, vol. 28, no. 4, pp. 585–594, Apr. 2009.

[47] Z. Guo, C. Li, L. Song, and L. V. Wang, "Compressed sensing in photoacoustic tomography *in vivo*," *J. Bio. Opt.*, vol. 15, no. 2, p. 021311, 2010.

[48] M. M. Baskaram and R. Bordawekar, "Optimizing sparse matrix-vector multiplication on GPUs," IBM, Armonk, NY, Tech. Rep. RC24704, 2008.

Authors' photographs and biographies not available at the time of publication.